8

Epitaxial (Ba,Sr)TiO_3 Ferroelectric Thin Films for Integrated Optics

D. Y. Wang and S. Li
School of Materials Science and Engineering, The University of New South Wales, Sydney, Australia

1. Introduction

Complex ferroelectric oxides with excellent optical properties and strong electro-optic (E-O) effects have now opened up the potential for guided-wave devices used in multifunctional integrated optics (Wessels, 2007). Since an applied electric field can result in a change in both the dimensions and orientation of the index ellipsoid of the material through the E-O effect, the E-O effect affords convenient and widely used means of controlling the phase or intensity of the optical radiation. Electro-optic modulators, in particular operating at near infrared wavelengths of 1-1.6 μm, are essential for high-speed and wide bandwidth optical communication systems and ultrafast information processing applications (Tang et al., 2005). Bulk ferroelectric single crystals and transparent ceramics, e.g. $LiNbO_3$ (Gopalakrishnan et al., 1994; Wooten et al., 2000) and (Pb,La)(Zr,Ti)O_3 (Chen et al., 1980; Haertling, 1987), are commonly used. However, the realization of thin film E-O devices is of strong scientific and technological interest, since they require relatively low driving power and possess higher interaction efficiency in comparison to bulk modulators. The use of thin films in E-O devices can clearly lead to geometrical flexibility and ability to grow waveguides on diverse substrates for possible integration with existing semiconductor technologies to produce devices much smaller than bulk hybrid counterparts.

In spite of its promise, ferroelectric thin films for optical applications are not well developed. This results from numerous requirements on material perfection for optical devices. At present, only a few laboratories have succeeded to partially master the thin film technology for the optical devices (Guarino et al. 2007; Masuda et al. 2011; Nakada et al. 2009; Petraru et al. 2002; Suzuki et al. 2008), but steady progress is visible. A typical thin film E-O modulator concept comprises: (1) a ferroelectric thin film layer with high E-O coefficient; (2) for waveguide devices, the ferroelectric thin film needs to be optically transparent preferably with low optical loss. Thus heteroepitaxial deposition is required; (3) the epitaxial ferroelectric film must be deposited on substrates with a lower refractive index than the layer itself for a strong light confinement and high optical power density; (4) the waveguide modulator structure, for instance, a Mach-Zehnder geometry, has to be patterned by lithography and etching and also top cladding and electrodes need to be deposited.

Great efforts have been made to explore suitable ferroelectric oxide materials that have large E-O coefficient and can be epitaxially grown on low-refractive-index substrates. To date, the

most widely studied ferroelectrics for E-O applications are the titanates and niobates, including $BaTiO_3$ (Kim & Kwok, 1995), $PbZr_xTi_{1-x}O_3$ (Kang et al., 2008; Zhu et al., 2010), $(Pb,La)(Zr,Ti)O_3$ (Adachi & Wasa, 1991; Masuda et al., 2010; Uchiyama et al., 2007), $LiNbO_3$ (Lee et al., 1996), $KNbO_3$ (Graettinger et al. 1991), $(K,Na)NbO_3$ (Blomqvist et al., 2005), $KTa_xNb_{1-x}O_3$ (Hoerman et al., 2003), $Sr_xBa_{1-x}Nb_2O_6$ (Tayebati et al., 1996) and $Pb(Mg_{1/3}Nb_{2/3})O_3$-$PbTiO_3$ (Lu et al., 1998, 1999) etc. Recently, the deposition of ferroelectric oxide thin films by a variety of techniques have been explored including molecular beam epitaxy (MBE), pulsed laser deposition (PLD), sputtering, sol-gel and metal-organic chemical vapor deposition (MOCVD) (Wessels, 2007). In contrast to other methods, PLD permits a stoichiometric transfer of material from the target to the film and film growth at high temperatures in reactive ambient gas, in particular, oxygen. However, to produce high quality thin films with good optical transparency and low optical loss for waveguide applications is still a very challenging task. $Ba_{1-x}Sr_xTiO_3$, abbreviated as BST, traditionally considered as an excellent microwave material for wide applications in wireless communication due to its large dielectric tunability at GHz regime, attracts much attention in optoelectronic community because of its high E-O coefficients (Kim et al., 2003; Li et al., 2000; Wang et al., 2007a, 2010). For integration, the films are not only required to have E-O properties that are comparable to those of the bulk but also must have a high degree of microstructure perfection in order to minimize optical scattering losses. In this case, the optical propagation loss has been the most serious barrier for practical applications of ferroelectric thin films to waveguide devices. Hence it must be reduced below a level of about 1 dB/cm for practical applications (Wessels et al., 1996). $Ba_{1-x}Sr_xTiO_3$ thin films have been proved to possess high optical transparency and acceptable optical loss (Wang et al., 2006a), which makes $Ba_{1-x}Sr_xTiO_3$ a very promising candidate for active waveguide applications. Furthermore, $Ba_{1-x}Sr_xTiO_3$ thin films have potential to overcome the major drawbacks of E-O ferroelectric materials, such as the high cost and long optical path length of $LiNbO_3$ and $LiTaO_3$ single crystals and the environmental burden of lead content in $(Pb,La)(Zr,Ti)O_3$ transparent ceramics and thin films.

In this chapter, $Ba_{0.7}Sr_{0.3}TiO_3$ ferroelectric thin films with large E-O effect were epitaxially grown on single-crystal MgO substrates by pulsed laser deposition technique and the important issues of their material properties are tackled. $Ba_{0.7}Sr_{0.3}TiO_3$/MgO rib-type waveguides and Mach-Zehnder modulators are designed, fabricated and characterized.

2. $Ba_{0.7}Sr_{0.3}TiO_3$ thin film deposition

Orientation engineered $Ba_{0.7}Sr_{0.3}TiO_3$ thin films with surface normal orientations of [001], [011] and [111] have been epitaxially deposited on optically double-side polished single-crystal MgO [001], [011] and [111] substrates, respectively, by pulsed laser deposition using a KrF excimer laser (Lambda Physik COMPex 205) with a wavelength of 248 nm, a pulse width of 28 ns and a repetition rate of 10 Hz. The laser beam impacts the rotating stoichiometric target with an energy density of 2 J /cm^2. The distance between the target and the substrate was fixed at 5 cm, while the substrate temperature was maintained at 750 ^{o}C. All films were prepared in an oxygen atmosphere with partial pressure of 27 Pa. The growth conditions used in this work have been optimized and summarized in Table 1.

The crystal structures of the $Ba_{0.7}Sr_{0.3}TiO_3$ thin films were examined using an X-ray diffractometer equipped with Cu Kα radiation. The θ/2θ scan patterns of [001], [011] and

Target- substrate distance	50 mm
Laser energy	250 mJ
Repetition rate of pulsed laser	10 Hz
Ambient gas	O_2
Total pressure of ambient gas	200 mTorr
Substrate temperature	750 °C
Growth rate	~ 20 nm/min

Table 1. PLD conditions of $Ba_{0.7}Sr_{0.3}TiO_3$ thin films.

[111]-oriented $Ba_{0.7}Sr_{0.3}TiO_3$ films on [001], [011] and [111] MgO substrates, respectively, are shown in Fig. 1 (a)-(c). No secondary orientations and phases can be seen in any of the three XRD patterns, indicating the BST films are oriented along the particular normal of the substrates with a pure perovskite phase. The full width at half maximum (FWHM) of the x-ray rocking curves (ω scan) for the BST [001], [011] and [111] peaks of the [001], [011] and [111]-oriented BST films are 0.46°, 0.57° and 1.06°, respectively, implying that the crystallites of all three films are fairly well ordered. The in-plane texturing of the BST thin films with respect to the major axes of the MgO substrates was confirmed by the XRD φ scan of the BST [110], [010] and [100] reflections of the [001], [011] and [111]-oriented BST films. The peaks from BST films coincide in position well with those from MgO substrates, as shown in Fig. 1 (e)-(f), which suggests a nonlattice–rotated epitaxial growth of all the as-deposited BST films. For the optical applications, epitaxial growth is strongly desirable because of the basic requirements for the reduction of light scattering associated with the refractive index mismatch at grain boundaries (Lee et al., 1996) as well as the E-O properties comparable to the bulks (Wessels, 2004).

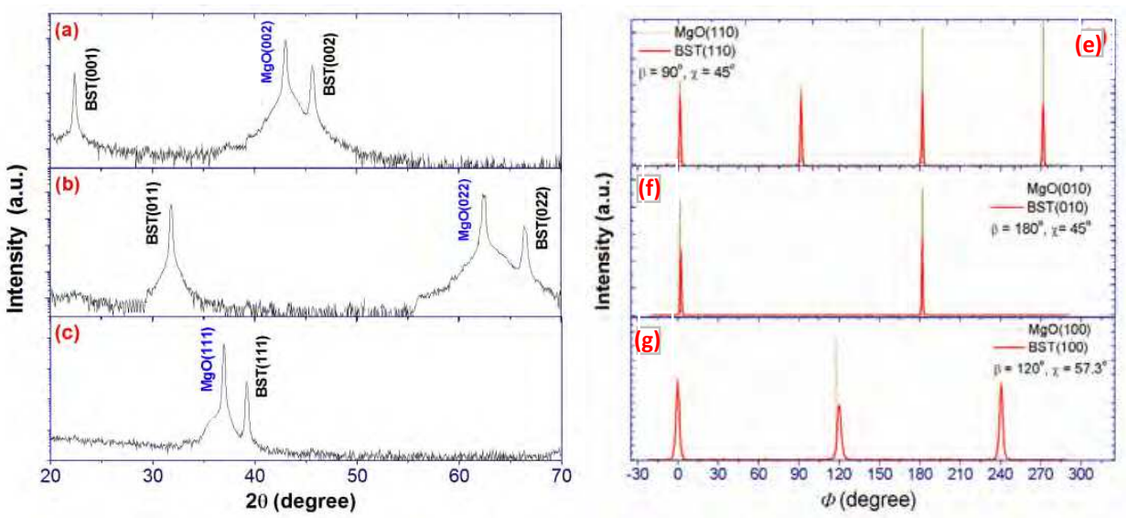

Fig. 1. XRD θ/2θ scan patterns of $Ba_{0.7}Sr_{0.3}TiO_3$ thin films deposited on (a) MgO [001], (b) MgO [011] and (c) MgO [111] single crystal substrates; XRD φ scans of (e) $Ba_{0.7}Sr_{0.3}TiO_3$ [110] and MgO [110] reflections of [001]-oriented film (f) $Ba_{0.7}Sr_{0.3}TiO_3$ [010] and MgO [010] reflections of [011]-oriented film and (f) $Ba_{0.7}Sr_{0.3}TiO_3$ [100] and MgO [100] reflections of [111]-oriented film, providing nonlattice-rotating epitaxial growth of $Ba_{0.7}Sr_{0.3}TiO_3$ thin films. [Reproduced with permission from Ref. (Wang et al., 2010). Copyright 2010, AIP]

3. Optical properties of $Ba_{0.7}Sr_{0.3}TiO_3$ thin films

3.1 Optical transmittance and band gap energy

Optical constants can be evaluated using the "envelop method" developed by (Manifacier et al, 1976). For an insulating film on a transparent substrate, assuming the film is weakly absorbing and the substrate is completely transparent, the optical band gap energy E_{gap} and refractive index n can be derived from the transmission spectra. The optical transmission of the $Ba_{0.7}Sr_{0.3}TiO_3$ thin films was measured using a Perkin Elmer (precisely) Lambda 950 UV-VIS spectrometer in the wavelength range of 200-2000 nm. All three BST films are highly transparent in the visible to near infrared regions, as shown in Fig. 2, which is favorable for applications in optical communication (e. g. λ = 1.3 and 1.5 μm). The transparency of the films drops sharply in the UV region and the threshold wavelength is located at 311, 319 and 317 nm for [001], [011] and [111]-oriented films, respectively. The optical band gap energy E_{gap} of a thin film can be deduced from the spectral dependence of the absorption constant $\alpha(\upsilon)$ by applying the Tauc relation (Tauc, 1972):

$$\alpha h\upsilon = const(h\upsilon - E_{gap})^{1/r} \tag{1}$$

where υ is the frequency and h is the Planck's constant, r = 2 for a direct allowed transition. The absorption constant $\alpha(\upsilon)$ is determined from the transmittance spectrum using the relation (Davis & Mott, 1970):

$$\alpha(\upsilon) = [\ln\frac{1}{T(\upsilon)}] / d \tag{2}$$

where $T(\upsilon)$ is the transmittance at frequency υ and d is the film thickness. Thickness of the BST thin films were measured by alpha-step profiler. (187, 193 and 225 nm for [001], [011]

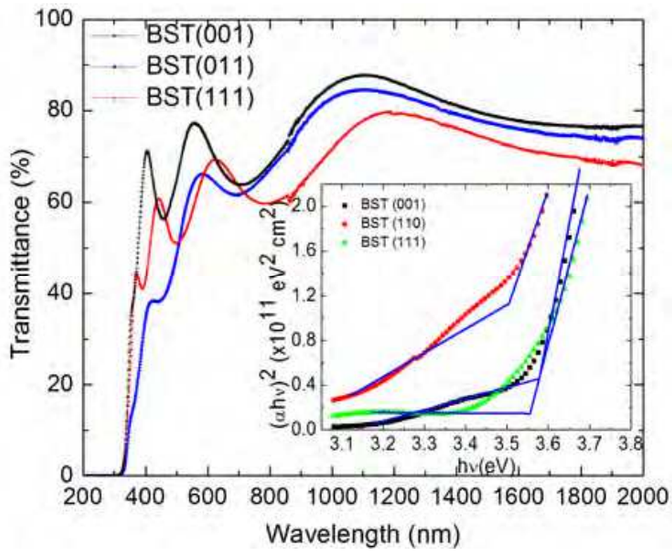

Fig. 2. Optical transmission spectra of [001], [011] and [111]-oriented $Ba_{0.7}Sr_{0.3}TiO_3$ thin films. Inset is the plots of $(\alpha h\upsilon)^2$ versus hυ for $Ba_{0.7}Sr_{0.3}TiO_3$ thin films. The optical band gap energy E_{gap} is deduced from extrapolation of the straight line to $(\alpha h\upsilon)^2 = 0$. [Reproduced with permission from Ref. (Wang et al., 2010). Copyright 2010, AIP]

and [111]-oriented films, respectively). The optical band gap energy is then obtained by applying a "base line" method (Marple, 1966) in order to minimize the impact of reflectance losses at air-film and film-substrate interfaces. Inset of Fig. 2 shows the plots of $(\alpha h\upsilon)^2$ versus $h\upsilon$ for $Ba_{0.7}Sr_{0.3}TiO_3$ thin films grown on MgO substrates. The optical band gap energies are found to be 3.57 ± 0.01, 3.50 ± 0.02 and 3.55 ± 0.01 eV for for the [001], [011] and [111] oriented films, respectively. It is discernable that the absorption edges and optical band gap energy of the $Ba_{0.7}Sr_{0.3}TiO_3$ films are orientation dependent. Although the grain size effect on optical band gap energy of BST thin films has been reported (Thielsch et al.,1997), it is believed that orientation is the predominant factor that is responsible for the observed difference of E_{gap} in our case, as the average crystallites dimensions estimated by Scherrer's formula for the three films are comparable. Similar orientation dependence of band gap energy has also been observed in other oxygen-octahedral perovskite ferroelectrics, such as $Pb(Mg_{1/3}Nb_{2/3})O_3$-$PbTiO_3$ (Wan et al., 2005) etc.

The refractive index n of the as-deposited BST films was derived on the basis of the following expressions (Manifacier et al., 1976),

$$n = \sqrt{N' + \sqrt{N'^2 - n_s^2}} \tag{3}$$

$$N' = \frac{1 + n_s^2}{2} + \frac{2n_s(T_{\max} - T_{\min})}{T_{\max}T_{\min}} \tag{4}$$

in which $T_{\max}$ and $T_{\min}$ are the corresponding maximum and minimum of the envelop around the interference fringes at a certain wavelength λ, n_s is the refractive index of MgO, which is taken from Ref. (Bass, 1994) based on Sellmeier dispersion equation. The experimental values of the refractive index are found to fit closely to a Cauchy function as a formula:

$$n = A + (B/\lambda)^2 + (C/\lambda)^4 \tag{5}$$

where A, B, C are determined from fits to the experimental spectra. The calculated n and the dispersion of the refractive index for the three BST thin films were given in Fig. 3. The dispersion curves rise rapidly towards shorter wavelengths, showing the typical shape of dispersion near an electronic interband transition. Conspicuous orientation dependence of refractive index is discernable, especially in near infrared region. The [001]-oriented film exhibits the highest refractive index in near IR. The optical properties of an oxygen-octahedral ABO_3 perovskite ferroelectric are dominated by BO_6 octahedra, which govern the low-lying conduction bands and the highest valence bands. This lowest energy oscillator is the largest contributor to the dispersion of the refractive index (Chan et al., 2004). Meanwhile, voids caused by surface roughness and porosity inside the film is another controlling factor for the variation of refractive index (Chan et al., 2004; Yang et al., 2002). Moreover, changes in electronic structure due to lattice distortion and some variations of atomic coordination caused by the substrate orientations (Tian et al., 2002) may also be responsible for the observed variation in refractive index of differently oriented BST thin films.

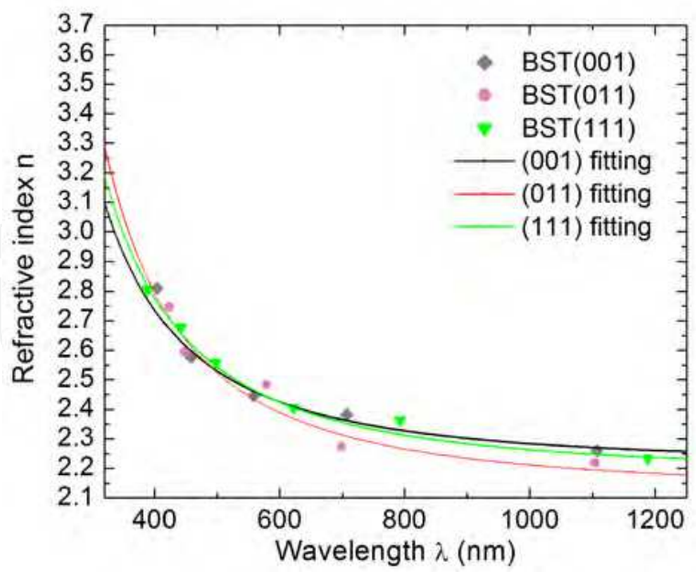

Fig. 3. Variation of refractive indices of [001], [011] and [111]-oriented $Ba_{0.7}Sr_{0.3}TiO_3$ thin films as a function of wavelength. The solid lines are the fitting curves based on Cauchy equation. [Reproduced with permission from Ref. (Wang et al., 2010). Copyright 2010, AIP]

3.2 Electro-Optic properties

Although the E-O properties of bulk ferroelectric materials, such as single crystals of $LiNbO_3$ and $BaTiO_3$, and PLZT transparent ceramics, are well identified, the identification of the E-O properties of ferroelectric thin films is not easy since they exhibit processing-dependent properties (Nashimoto et al., 1999) and crystallographic anisotropy (Wang et al., 2010). The E-O properties of the $Ba_{0.7}Sr_{0.3}TiO_3$ thin films were measured with a transverse geometry at the wavelength of 632.8 nm using modified Sénarmont method. The electrode pattern used for E-O characterization consisted of two coplanar electrodes, with dimensions 1.0 × 8.0 mm^2 separated by a 20-μm-wide gap. The experimental arrangement for E-O measurement is illustrated in Fig. 4. The film surface was set with the direction perpendicular to the incident light and the electric field was applied normal to the incident light beam. The light beam from a 2 mW stabilized He-Ne laser, after passing through a polarizer set at -45°, impinged normally on the film in the gap between two gold electrodes. The laser beam was then modulated at 50 kHz by the PEM-90 photoelastic modulator and then passed through an analyzer set at + 45°. The transmitted laser beam was detected by a photomultiplier tube (PMT). The electrical signal from the PMT was filtered by a band-pass filter and then fed to a SRS SR830 DSP lock-in amplifier. An electric field was then applied. The general expression for the light intensity I at the detector is given by:

$$I = 1 - \cos(B)\cos(A) + \sin(B)\sin(A) \tag{6}$$

where B is the phase retardation in the film sample, $A = A_0\cos(\Omega t)$ is the phase retardation in PEM-90 photoelastic modulator. A Fourier series expansion yields:

$$I = [1 - \cos(B)J_0(A_0)] + 2\sin(B)J_1(A_0)\cos(\Omega t) + 2\cos(B)J_2(A_0)\cos(2\Omega t) + \ldots \tag{7}$$

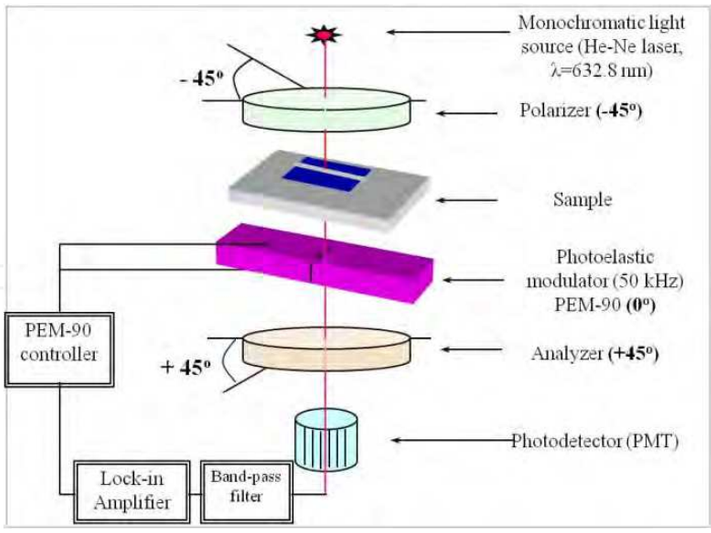

Fig. 4. Schematic diagram showing the modified Sénarmont method for the measuring E-O coefficients of thin films. [Reproduced with permission from Ref. (Wang et al., 2007a). Copyright 2007, AIP]

where $J_n(A_0)$ are the Bessel functions and the first, second and third terms represent the DC term, the fundamental term and the first harmonic term, respectively. Therefore, the electrical signals corresponding to these three terms are:

$$V_{DC} = G[1 - \cos(B)J_0(A_0)] \tag{8}$$

$$V_{1(peak)} = 2G\sin(B)J_1(A_0)\cos(\Omega t) \tag{9}$$

$$V_{2(peak)} = 2G\cos(B)J_2(A_0)\cos(2\Omega t) \tag{10}$$

where G is a constant of proportionality. If A_0 is chosen such that $J_0(A_0)=0$, then the DC signal is independent of the sample retardation B. This occurs for $A_0=2.405$ radians. The DC signal may therefore be used to "normalize" the fundamental term:

$$\frac{V_{1(peak)}}{V_{DC}} = 2\sin(B)J_1(A_0) \tag{11}$$

In Eq. (6), $V_{1(peak)}$ is the peak voltage of the signal. However, the lock-in amplifier only gives the rms voltage V_{rms}. For sinusoidal waveforms, V_{rms} is given by:

$$V_{rms} = \frac{V_{(peak)}}{\sqrt{2}} \tag{12}$$

If we define a ratio R_{1f} as:

$$R_{1f} = \frac{V_{1(rms)}}{V_{DC}} = \sqrt{2}\sin(B)J_1(A_0) \tag{13}$$

then the phase retardation B is given by:

$$B = \sin^{-1}[\frac{R_{1f}}{\sqrt{2}J_1(A_0)}] = \sin^{-1}[\frac{R_{1f}}{\sqrt{2}J_1(2.405)}] = \sin^{-1}[\frac{R_{1f}}{\sqrt{2}\cdot(0.5191)}] \quad (14)$$

Then the electric field induced birefringence change $\delta(\Delta n)$ can be deduced from the phase change B:

$$\delta(\Delta n) = \frac{\lambda B}{2\pi \cdot d} \quad (15)$$

where d is the thickness of the film.

The field induced birefringence of the thin films was characterized as a function of d. c. electric field E at room temperature and the result is shown in Fig. 5, in which strong orientation dependence of E-O effect is clearly seen. E-O effect for the [011]-oriented film is relatively weak, while large birefringence changes $\delta\Delta n$ are revealed in [001] and [111]-oriented films. All the three films exhibit predominantly linear birefringence change with respect to the applied d. c. electric field. A slight hysteresis behavior is observed in the $\delta\Delta n$ versus E plots for [001]-oriented film, which is consistent with its enhanced ferroelectric properties (Wang et al., 2005). Generally, the birefringence shift due to linear E-O effect (Pockels effect) is given by Eq. (16) as following,

$$\delta\Delta n = \frac{1}{2} n^3 r_c E \quad (16)$$

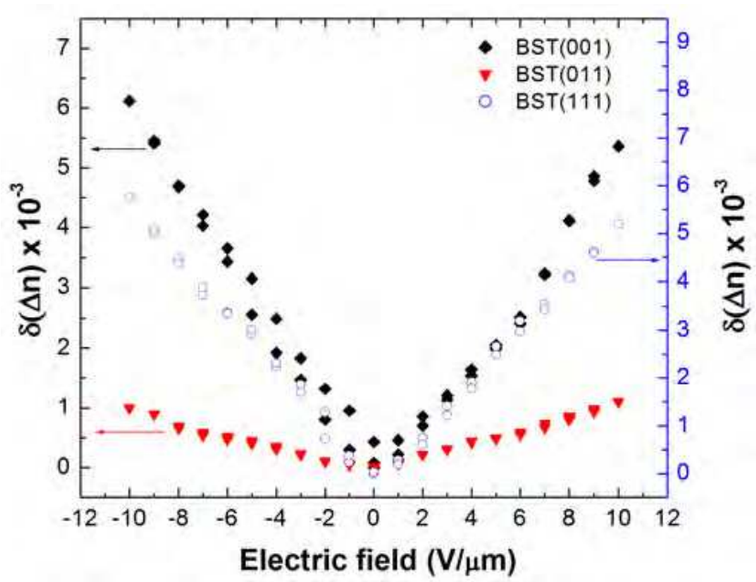

Fig. 5. Change in birefringence $\delta(\Delta n)$ as a function of applied d.c. electric field for [001], [011] and [111]-oriented $Ba_{0.7}Sr_{0.3}TiO_3$ thin films. The birefringence was determined at a wavelength of 632.8 nm. [Reproduced with permission from Ref. (Wang et al., 2010). Copyright 2010, AIP]

With this Eq. (16), the effective linear electro-optic coefficient r_c can be deduced from the slope of the $\delta\Delta n$ versus E plots. In this case, the linear E-O coefficient r_c of the [001], [011] and [111]-oriented BST thin films were calculated to be 99.1 pm/V, 15.7 pm/V and 87.8 pm/V, respectively. The difference in E-O properties in the three kinds of oriented BST films may be attributed to the changes in distribution and magnitude of spontaneous polarization (electric) in orientation engineered films. The polarization changes could originate from: (1) the magnitude variation of the relative displacement of the Ti^{4+} with respect to O^{2-} in the octahedral structure, (2) the change of domain growth mechanism, and (3) the lattice distortion caused by the stain in perovskite structure (Lu et al., 1999; Moon et al., 2003). Other factors, such as dielectric permittivity, may also be responsible for the orientation dependence of E-O effect in our tetragonal-distorted BST thin films (Wan et al., 2004). Nevertheless, the linear E-O coefficients r_c of [001] and [111]-oriented BST films are considerable higher than that of commonly used $LiNbO_3$ single crystals (30.8 pm/V) (Xu, 1991), showing their potential for use in active waveguide applications. The understanding of orientation dependent optical properties of BST thin films is technically important for practical optoelectronic device development. Due to its largest E-O coefficient, we will focus on [001]-oriented BST thin films in the following sections.

3.3 Light propagation characteristics

To characterize the waveguide properties of the $Ba_{0.7}Sr_{0.3}TiO_3$ films, prism coupling experiments were performed at wavelengths of both 632.8 nm and 1550 nm. Fig. 6 shows the guided mode spectra (m-lines) of a 620 nm thick $Ba_{0.7}Sr_{0.3}TiO_3$ thin film on MgO [001]

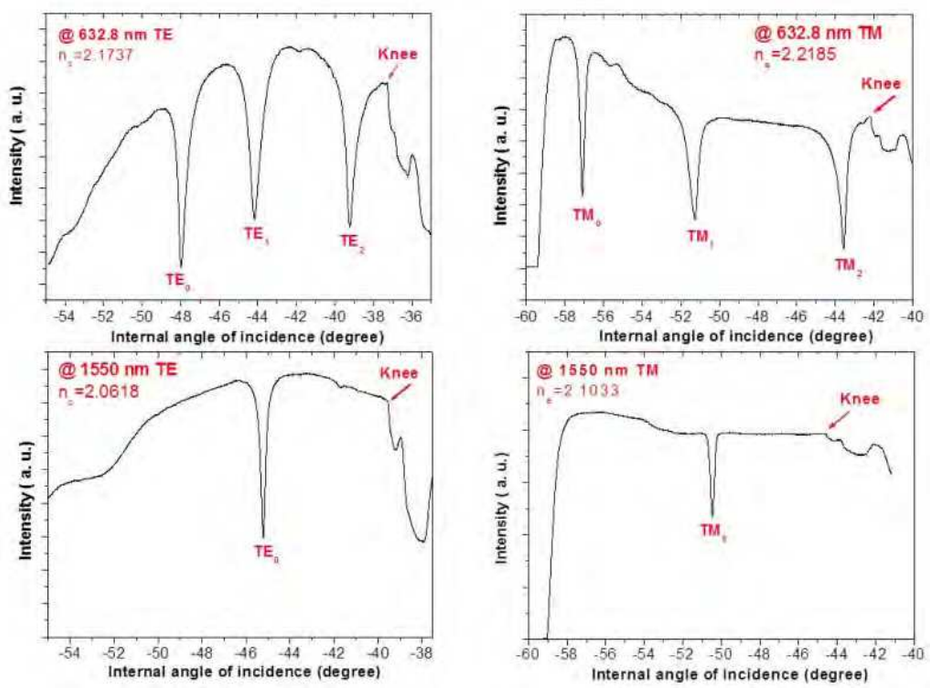

Fig. 6. Prism coupling spectra of the $Ba_{0.7}Sr_{0.3}TiO_3$ thin film (620 nm thick) epitaxially grown on MgO [001] substrate at both 632.8 nm and 1550 nm. [Reproduced with permission from Ref. (Wang et al., 2006a). Copyright 2006, OSA]

substrate measured by the prism coupler. Three TE (transverse electric) and three TM (transverse magnetic) modes were observed at 632.8 nm, while only a single TE and TM mode were found at 1550 nm. The peaks of each guided mode are very sharp and distinguishable, indicating that a good confinement of light propagation is achieved and the film is potentially useful for optical waveguide devices. The measured film thickness of 626.0 nm in the TE mode at 632.8 nm was in good agreement with that determined by an α-step profile measurement. At the wavelength of 632.8 nm, the refractive indices for TE and TM modes were determined to be 2.1696 and 2.2185, respectively, giving an index difference of 0.0489. The large index difference cannot be fully explained using the intrinsic birefringence in the film. Perhaps, this phenomenon is attributed to the strain induced by the lattice mismatching. The well-defined and relatively sharpen m-lines suggest that the optical losses in the film are rather low since the optical losses are related to the FWHM of the m-lines (Dogheche et al.; 2003Vilquin et al., 2003). It is obvious that the FWHM of m-lines at 1550 nm is smaller than that at 632.8 nm, a lower optical loss is expected at 1550 nm.

From the knowledge of the effective mode indices, it is possible to determine the refractive index profile along the film thickness direction for either TE or TM modes by using the inverse Wentzel-Kramers-Brillouin (i-WKB) method (Chiang, 1985). This method only depends on the refractive index distribution within the guiding layer. The refractive index profile of the $Ba_{0.7}Sr_{0.3}TiO_3$ thin film at 632.8 nm is shown in Fig. 7. It indicates a step-like index variation, which is synonymous with a good optical homogeneity along the BST film thickness. The refractive index remains constant within the guiding region and drops rapidly near the film-substrate interface. It is because plenty of lattice misfit induced dislocations exist near the film-substrate interface (Chen et al., 2002), thus degrading the optical properties at the interface.

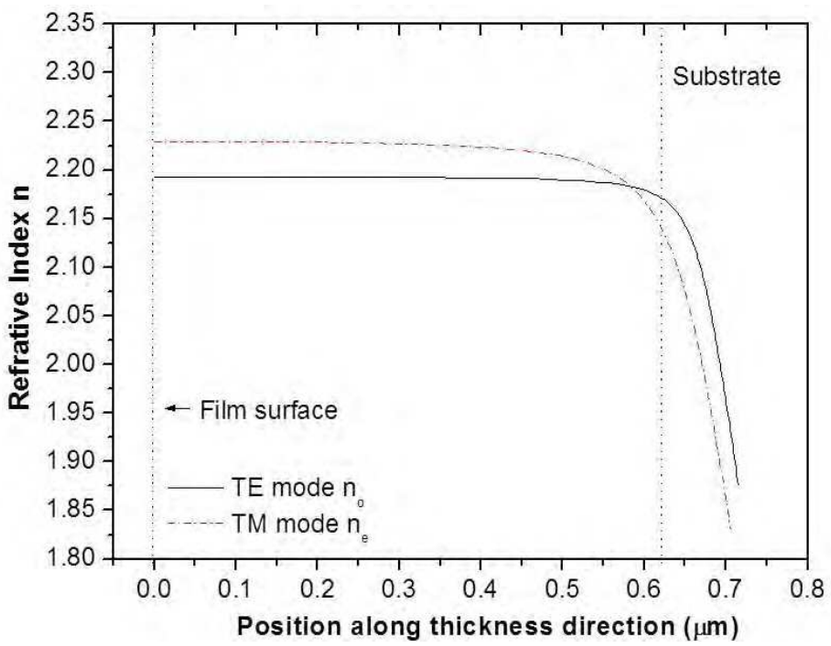

Fig. 7. Reconstruction of the refractive index profile of the $Ba_{0.7}Sr_{0.3}TiO_3$ thin film (620 nm thick) epitaxially grown on MgO [001] substrate at 632.8 nm using an i-WKB method. [Reproduced with permission from Ref. (Wang et al., 2006a). Copyright 2006, OSA]

3.4 Optical loss

For integration, the films are not only required to have E-O properties comparable to those of the bulk but also must have a high degree of microstructure perfection in order to minimize optical scattering losses. In this sense, the optical transparency is a demanding requirement for thin film waveguides and the optical propagation loss has been the most serious barrier for practical applications of ferroelectric thin films in the waveguide devices. Loss of about 2 dB/cm will reduce the efficiency of an optical device (e. g. frequency doublers) by over 50% (Fork et al., 1995). Nevertheless, investigations of the optical losses in ferroelectric thin films are insufficient. The optical loss is mainly caused by absorption, mode leakage, internal scattering and surface scattering. For a transparent ferroelectric thin film, the dominant loss mechanism is the scattering (Lu et al., 1998). In this study, a "moving fibre method" (build-in option of Metricon 2010 prism coupler) was employed to determine the surface scattering losses in the $Ba_{0.7}Sr_{0.3}TiO_3$ thin film (620 nm thick). The measurement setup is shown schematically in Fig. 8. In the moving fibre method, the exponential decay of light is measured by a fibre probe scanning down the length of the propagating streak. The optical fibre method is identical in concept to the CCD camera approach for measuring the decay of the propagating streak as described in previous work (Lu et al., 1998; Walker et al., 1994).

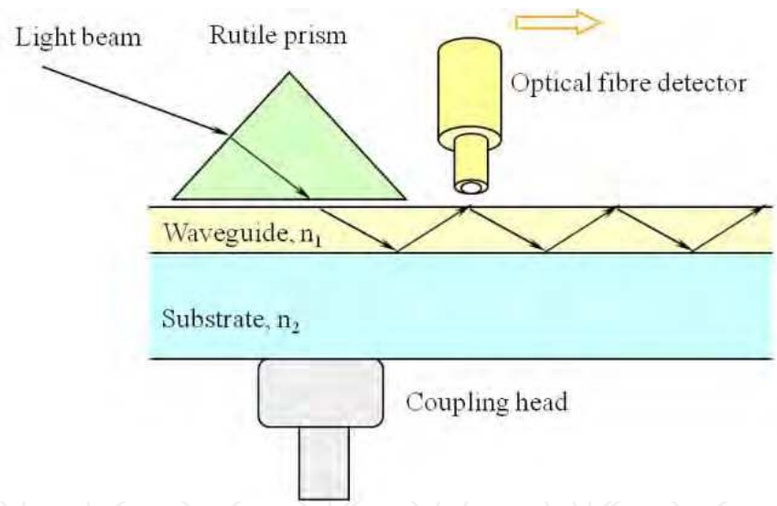

Fig. 8. A schematic diagram of the experimental arrangement for surface scattering loss measurements (moving fibre method). [Reproduced with permission from Ref. (Wang et al., 2006a). Copyright 2006, OSA].

The loss was derived for the film from measurements of the out-of-plane scattered light intensity for the specified guiding modes. Fig. 9 shows the scattered intensity from TE_0 and TM_0 modes at both 632.8 nm and 1550 nm. A least square fit gives the losses of 2.64 dB/cm and 3.04 dB/cm for TE_0 and TM_0 modes at 632.8 nm, respectively and 0.93 dB/cm and 1.29 dB/cm for TE_0 and TM_0 modes at 1550 nm, respectively. Losses with similar magnitude were measured for the other guided modes of the $Ba_{0.7}Sr_{0.3}TiO_3$ thin film as summarized in Table 2. For the modes of higher order, higher scattered losses were observed. It is noticeable that the scattered losses at 1550 nm for the commonly used wavelength in optical communication are rather low, which is consistent with our prediction using m-line

measurements. The accuracy of our loss results is limited due to the small sample area and thus the short scanning length along the light propagation direction. But it gives a good approximation and the results are comparable with previous reported data in ferroelectric thin films (Beckers et al., 1998; Lu et al., 1998; Walker et al., 1994).

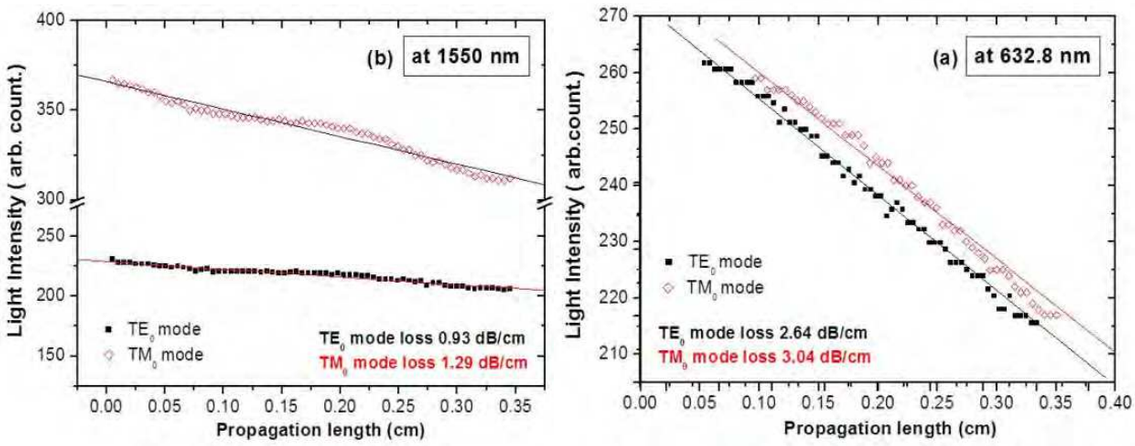

Fig. 9. Scattered intensity from the TE_0 and TM_0 modes of a 620 nm thick $Ba_{0.7}Sr_{0.3}TiO_3$ thin film epitaxially grown on MgO [001] substrate at both 632.8 nm and 1550 nm. [Reproduced with permission from Ref. (Wang et al., 2006a). Copyright 2006, OSA]

Losses / Guided mode	at 632.8 nm (dB/cm)	at 1550 nm(dB/cm)
TE_0	2.64	0.93
TE_1	6.43	--
TE_2	8.33	--
TM_0	3.04	1.29
TM_1	5.39	--
TM_2	8.85	--

Table 2. Surface scattered losses in $Ba_{0.7}Sr_{0.3}TiO_3$ thin film epitaxially grown on MgO [001] substrate.

4. Waveguide device design

For device speed and efficiency, the ideal waveguide structure should consist of a thin film material with a large E-O coefficient deposited onto a substrate possessing a small microwave dielectric constant (Lu et al., 1998). The thin films should have low optical loss and low surface roughness. Moreover, for better light confinement, a large refractive index difference between the substrate and the film is desired. Therefore, the BST/MgO configuration is a favorite structure for use in waveguide applications. In this work, the effective index method (Dogheche et al., 1996; Kogelnik & Ramaswamy, 1974; Ramaswamy, 1974) was employed to study the bidimensional waveguide. The physical structure of a BST/MgO ridge waveguide was schematically shown in Fig. 10.

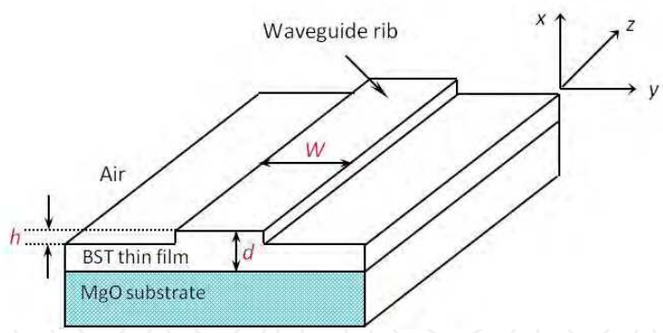

Fig. 10. Schematic structure of BST/MgO rib waveguide. [Reproduced with permission from Ref. (Wang et al., 2006b). Copyright 2006b, Elsevier]

For guide-wave applications, the design of a bidimensional waveguide begins with the optimization of the geometrical parameters of a planar waveguide. Consider the case of an asymmetric planar waveguide of an anisotropic active film with an isotropic cladding layer and a buffer layer. Since the film is highly oriented with the [001] direction parallel to the *x*-direction and the grain orientations in the *y* and *z* directions are completely random, we can assume that the average index in both *y* and *z* direction are the same, i.e., $n_y = n_z$, and the waveguide is therefore uniaxial. The dispersion equations for an asymmetric uniaxial planar thin film waveguide with an isotropic cover layer are given by:

$$kd\sqrt{n_y^2 - N_m^2} = m\pi + \sum_{i=1,2} \tan^{-1}\left(\sqrt{\frac{N_m^2 - n_i^2}{n_z^2 - N_m^2}}\right) \tag{17}$$

for the TE polarization and by

$$kd\sqrt{n_x^2 - N_m^2} = m\pi + \sum_{i=1,2} \tan^{-1}\left(\frac{n_y}{n_i}\right)^2\left(\sqrt{\frac{N_m^2 - n_i^2}{n_x^2 - N_m^2}}\right) \tag{18}$$

for the TM polarization. Where N_m is the effective index of the mode with the mode number m = 1, 2, 3 …, n_i is the index of the i^{th} layer, d is the film thickness and k (= $2\pi/\lambda$) is the free space wave number. To realize the bidimensional structure, the first step is to study the effect of the film thickness d on guided modes propagation. Fig. 11 shows the dispersion of the effective index N_m as a function of the guiding layer thickness d. For the planar guiding structure, we have studied the transverse confinement of the light. Therefore, we should consider only the TE polarization modes. In order to minimize the waveguide losses, it may be designed such that the transverse resonance condition could be satisfied; in order to allow only the TE_0 guided mode to propagate along the active layer. As shown in Fig. 11, the number of guided modes increases as the film thickness increases. At a wavelength of 1550 nm, the cutoff of TE_0 and TE_1 modes are 0.19 μm and 0.86 μm, respectively. In our study, a film thickness of 620 nm corresponds to a single-mode propagation at 1550 nm, resulting in the transverse confinement of the mode.

To establish both the horizontal and vertical guiding confinement of single propagation mode, the geometry of the rib (width W and height h) must be determined for a given film thickness d (=620 nm). For lateral confinement of the light, the evolution of effective index as

a function of the width W was calculated. We consider a rib waveguide as shown in Fig. 12 (a), where n_c, n_f and n_s are the refractive indices of the cladding layer, film and substrate with $n_f > n_c, n_s$. The basic idea is to replace the rib waveguide structure by a fictive equivalent planar waveguide with the effective indices N_{eff1} and N_{eff2} obtained from planar waveguides of thickness d and (d-h) as shown in Fig. 12 (b) and (c). Then the problem has been simplified to solving the "thickness" W in the lateral planar waveguide shown in Fig. 12 (c) for a given rib height h.

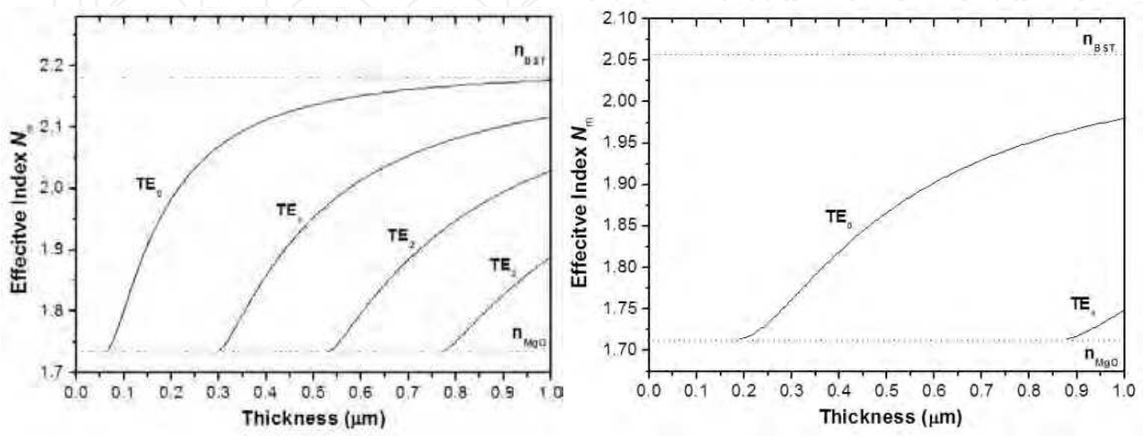

Fig. 11. Dispersion of effective index N_m of the modes versus the film thickness d for a BST/MgO structure. (a) λ = 632.8 nm, (b) λ = 1550 nm. [Reproduced with permission from Ref. (Wang et al., 2006b). Copyright 2006, Elsevier]

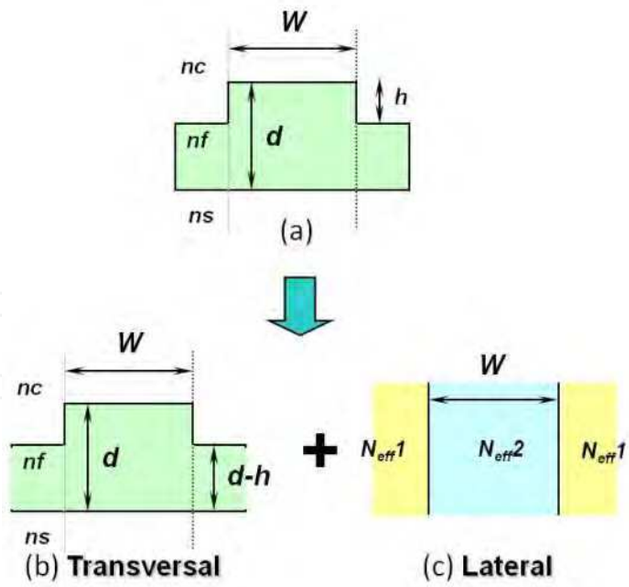

Fig. 12. Description of the effective index method for a rib waveguide. (a) the original rib waveguide; (b) solving the vertical slab problem to define N_{eff1} and N_{eff2}; (c) solving the equivalent horizontal slab problem to determine the N_{eff} of the whole structure. [Reproduced with permission from Ref. (Wang et al., 2006b). Copyright 2006, Elsevier]

Fig. 13 shows the simulation results of the evolution of the effective index as a function of the rib width *W* for some given rib height *h* at both 633 nm and 1550 nm, which gives a good description of the influence of rib geometry on the effective index in considering a lateral single-mode propagation. The useful region of the single-mode rib waveguide is a function of the geometrical parameters of the rib (*W* and *h*). The cut-off width of the TE_{01} mode depends on the value of height *h*. At λ=1550 nm, for *h* = 50 nm in Figure 6 (b), the waveguide becomes multimode for *W* greater than 2.4 μm. Actually, for a deeper height *h*, the width *W* has to be narrower to maintain a single-mode lateral propagation. Meanwhile, a larger rib height may cause serious scattering loss if optical scattering from the sidewall of the waveguide is significant. Although the accuracy of cut-offs calculated by effective index method needs to be improved, it does provide a good reference and approximation for us to shape the waveguide geometry far from the cut-offs in order to achieve a single-mode rib waveguide.

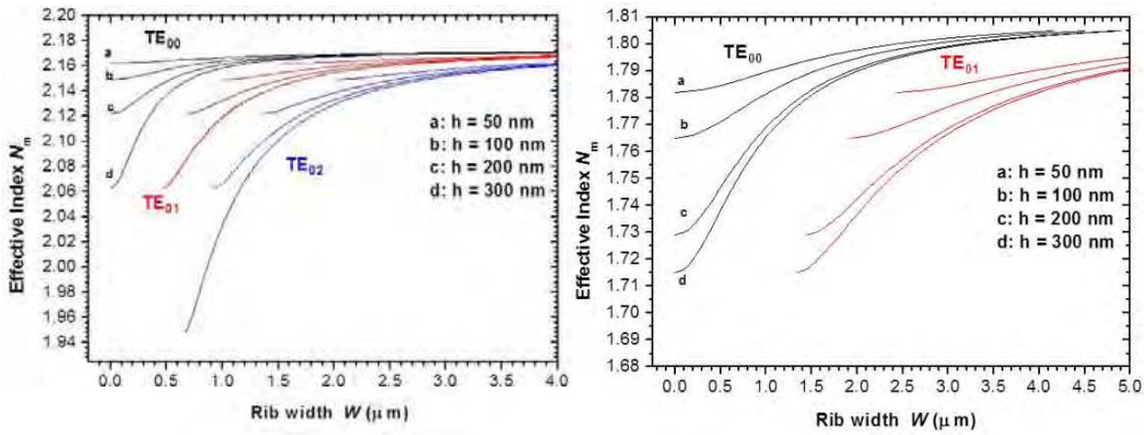

(a) (b)

Fig. 13. Effective index N_m versus rib width *W* for various heights *h* of a BST/MgO rib waveguide. (a) λ = 632.8 nm, (b) λ = 1550 nm. [Reproduced with permission from Ref. (Wang et al., 2006b). Copyright 2006, Elsevier]

In integrated optics, interferometric devices such as optical sensors and electro-optic amplitude modulators are often of the Mach-Zehnder interferometer (MZI) type (Krijnen et al., 1995). The proposed structure of the $Ba_{0.7}Sr_{0.3}TiO_3$ Mach-Zehnder modulator investigated in this work is shown schematically in Fig. 14. The modulator consists of an input waveguide that branches out into two separate parallel waveguides that are finally recombined into the output waveguide. By applying a voltage to the coplanar electrodes, the phase of the guided light in this branch can be changed. All the waveguides in the modulator are of the rib type and the geometry of the rib is chosen based on the numerical calculation in order to achieve single mode propagation at a wavelength of 1550 nm. The active arm length and the device length are set at 5000 μm and 9000 μm, respectively, to assure smooth curvatures at the Y-branches. In practice, the branching angle is usually kept below 1° in order to reduce the insertion loss because the loss increases with branching angle (Agrawal, 2004). However, due to the limited length (1 cm) of our thin film samples, the branching angle is set at 3°.

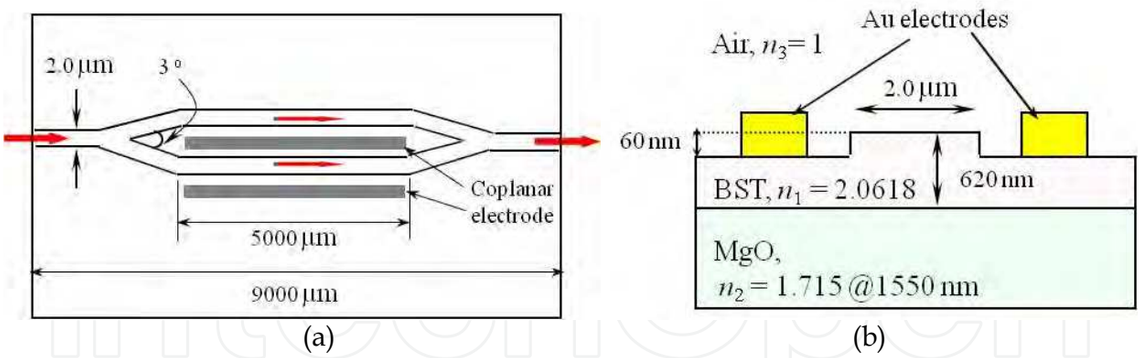

Fig. 14. Geometry of the investigated BST/MgO Mach-Zehnder E-O modulator. (a) Planar view; (b) Cross-sectional view of the active arm.

5. Waveguide device processing

To fabricate a rib waveguide from BST thin film, the process includes standard photolithographic patterning and dry etching. The microfabrication flow chart is shown in Fig. 15. After cleaning the film surface, a 150 nm thick chromium film was deposited on the $Ba_{0.7}Sr_{0.3}TiO_3$ film by rf magnetron sputtering to serve as the etch barrier layer. A positive photoresist was then deposited on the chromium layer by spin coating, resulting in a photoresist layer of 1 μm thickness. After baking, the photoresist layer was exposed under a mask to high intensity ultraviolet light in a mask aligner. The exposed photoresist was then immersed in a developer to release the desired waveguide pattern. Using an etching solution of $Ce(NO_3)_4$ in aceric acid, the chromium layer without the protection of photoresist was removed, leaving the bare waveguide patterns of the undeveloped photoresist covering the chromium barrier layer on the film surface.

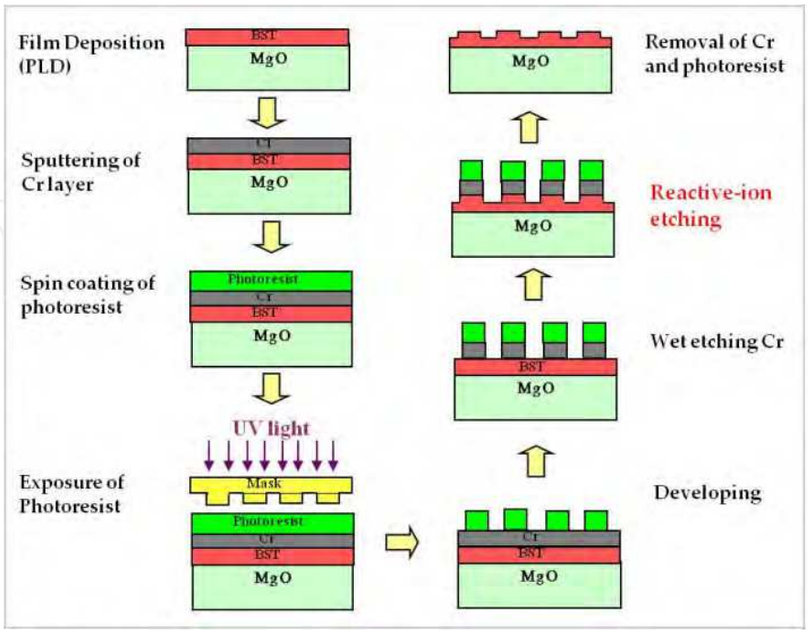

Fig. 15. Microfabrication flow chart of thin film rib waveguides.

Dry etch of the BST layer was performed using reactive ion etching in a CF_4/Ar ambient. A rf power of 200 W was used and the gas pressure was kept at 4.7 Pa. A 30-min etching results in ~ 60 nm depth as measured using an alpha-step surface profiler. Fig. 16 shows the SEM image of a cleaved BST/MgO rib waveguide. It is clearly seen that geometry of the rib is 620 nm of thickness, 60 nm of etched depth and 1.9 μm of width. These dimensions meet the requirements for a single-mode ridge waveguide at 1550 nm based on the theoretical calculation so that a single-mode propagation along the rib is expected. For Mach-Zehnder modulators, Au top electrode layer of 150 nm thick was deposited by rf magnetron sputtering, followed by a photolithographic patterning and wet chemical etching. The coplanar electrodes length and gap were 5.0 mm and 10 μm, respectively. The modulator was oriented along the BST [110] direction.

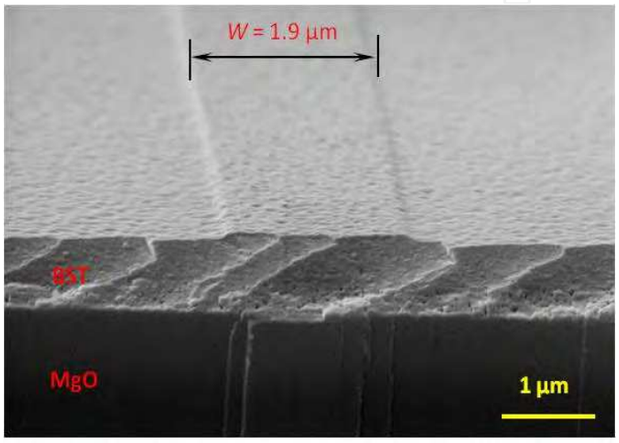

Fig. 16. SEM image of a cleaved BST/MgO rib waveguide. [Reproduced with permission from Ref. (Wang et al., 2006b). Copyright 2006, Elsevier]

6. Characterization of rib waveguide and Mach-Zehnder modulator

The near-field output pattern of the BST/MgO rib waveguide was measured using an end-fire coupling technique (Wang et al., 2006b). Fig. 17 shows a schematic diagram of the end-fire coupling method. Light source is a TE-polarized semiconductor laser with a wavelength of 1550 nm. A polarization-maintaining single mode fibre was used for input and butt-coupled to the cleaved endface of the waveguide. A charge-coupled device (CCD) camera was used to image the output pattern of the waveguide through a micro-objective lens. Fig. 18 shows the near-field output pattern of the BST/MgO rib waveguide. It illustrates that the output intensity is a single mode beam with Gaussian beam profile, showing that a strong light beam is propagating along the rib structure.

The Mach-Zehnder modulator was first tested without applying electric field using the end-fire coupling method at a wavelength of 1550 nm to confirm its single propagation mode characteristics. The E-O response (modulation of light intensity) of the $Ba_{0.7}Sr_{0.3}TiO_3$ Mach-Zehnder modulator was characterized using the setup shown in Fig. 19 (Wang et al., 2007b). A light beam (λ = 1550 nm) from a laser diode was coupled into a single-mode optical fibre. A fibre polarizer was used for defining the polarization state of the input light (TE). The light beam was end-fire coupled into the Mach-Zehnder modulator. The output of the waveguide was butt-coupled into another single mode fibre, which was fed to an IR

photodetector and then to an optical spectrum analyzer. Two *xyz* micro-positioning systems were used to position the optical fibres at the input and output of the modulator. Contact needles, supported by micromanipulators, were used to apply the voltage to the coplanar electrodes. The transmitted optical intensity was recorded by an oscilloscope. The half-wave voltage V_π was determined to be 60 V by applying dc bias field to the modulator. To evaluate the electro-optic modulation under an ac electric field, a triangular voltage with a frequency of 25 Hz and peak voltage of 120 V was applied to the Mach-Zehnder modulator.

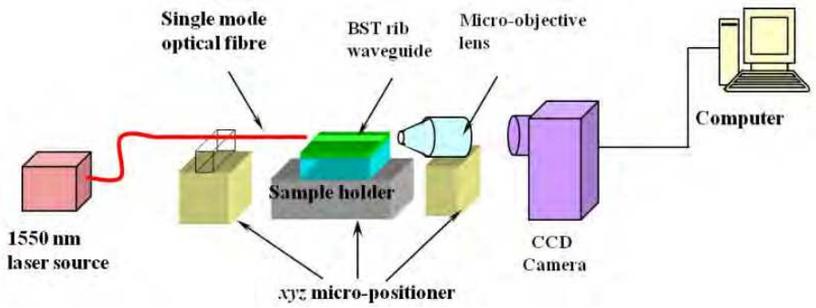

Fig. 17. Schematic diagram showing the measurement of the near-field output pattern by the end-fire coupling method. [Reproduced with permission from Ref. (Wang et al., 2006b). Copyright 2006, Elsevier]

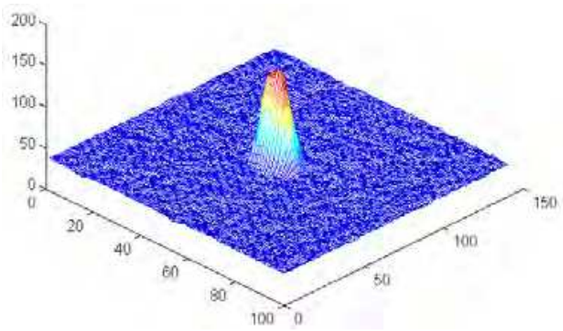

Fig. 18. The output light intensity exhibits a Gaussian profile, showing that only a single TE_{00} mode propagates along the BST/MgO rib waveguide at a wavelength of 1550 nm. [Reproduced with permission from Ref. (Wang et al., 2006b). Copyright 2006, Elsevier]

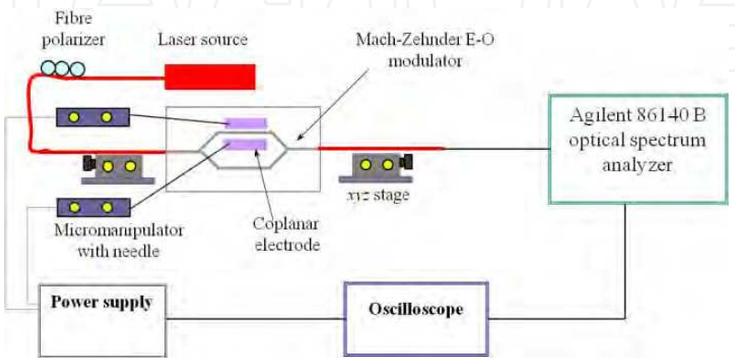

Fig. 19. Experimental setup for the characterization of Mach-Zehnder E-O modulator. [Reproduced with permission from Ref. (Wang et al., 2007b). Copyright 2007, Taylor & Francis]

The device exhibited good response to the applied ac voltage as shown in Fig. 20. A frequency doubling phenomenon was observed in the output signal as compared with the driving voltage. The performance of the device was very stable up to a frequency of 1 MHz. The E-O coefficient of the $Ba_{0.7}Sr_{0.3}TiO_3$ thin film Mach-Zehnder modulator can be calculated from the half-wave voltage V_π. Since $Ba_{0.7}Sr_{0.3}TiO_3$ thin film grown on MgO [001] substrate exhibits the linear E-O effect, the phase change B in the device can be derived from Eqs. (19) and (20):

$$B = \frac{2\pi L}{\lambda}\delta(\Delta n) = \frac{2\pi L}{\lambda}\cdot(\frac{1}{2}n^3 r_c^{eff} E) = \frac{\pi \cdot n^3 L V}{\lambda s} r_c^{eff} \tag{19}$$

where L is the activation length of the device, s is the coplanar electrode gap spacing, λ the wavelength of the light, V the applied voltage, and r_c^{eff} is the effective E-O coefficient. Putting $B = \pi$,

$$r_c^{eff} = \frac{\lambda \cdot s}{n^3 L V_\pi} \tag{20}$$

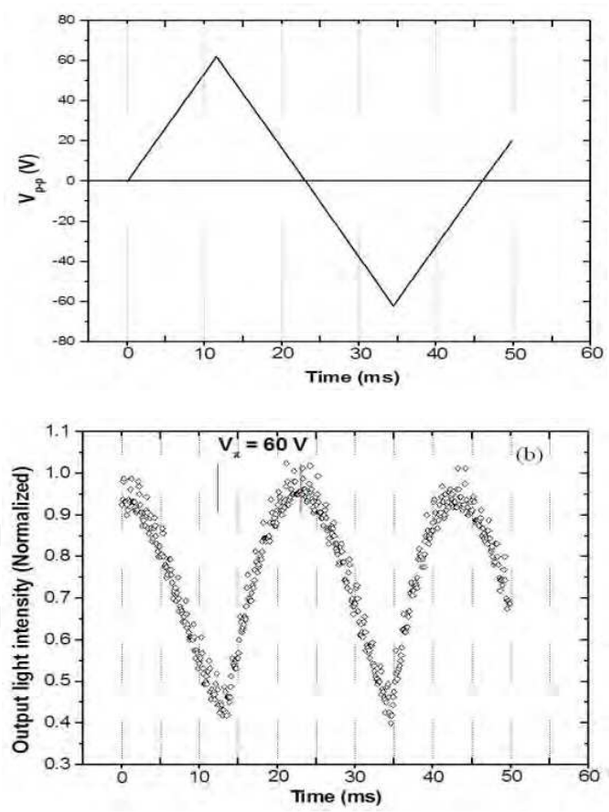

Fig. 20. E-O response of the BST/MgO Mach-Zehnder modulator when an ac voltage is applied. Upper trace is the applied 25 Hz trianglar driving voltage on 5.0-mm-long electrode; Bottom trace is the intensity modulation output signal at a wavelength of 1550 nm. [Reproduced with permission from Ref. (Wang et al., 2007b). Copyright 2007, Taylor & Francis]

Therefore, the effective E-O coefficient of the device at λ = 1550 nm is calculated to be r_c^{eff} = 27.0 × 10^{-12} m/V, which is comparable to that obtained for $LiNbO_3$ E-O modulators (Yariv & Yeh, 1983).

7. Conclusions

In summary, we studied the optical and electro-optic properties of ferroelectric $Ba_{0.7}Sr_{0.3}TiO_3$ thin films grown on MgO single-crystal substrates by pulsed laser deposition. XRD examination confirmed an epitaxial growth and a pure perovskite phase with good single crystal quality. The thin films possess excellent optical clarity with high optical transmission in visible light – near infrared regime. E-O properties of the $Ba_{0.7}Sr_{0.3}TiO_3$ thin films were measured at a wavelength of 632.8 nm through a modified Sénarmont method. A strong correlation between the optical, electro-optic properties and the crystalline orientation of epitaxial $Ba_{0.7}Sr_{0.3}TiO_3$ thin films were revealed. The linear electro-optic coefficient r_c of the [001], [011] and [111]-oriented thin films were found to be 99.1 pm/V, 15.7 pm/V and 87.8 pm/V, respectively. Understanding of the optical and electro-optic anisotropy in ferroelectric thin films is a critical issue for the device design and fabrication. Because of its largest E-O coefficient, the [001]-oriented $Ba_{0.7}Sr_{0.3}TiO_3$ thin films have been identified to be the most promising candidate for the integrated optics applications.

Waveguide characteristics of the [001]-oriented $Ba_{0.7}Sr_{0.3}TiO_3$ thin films were determined using prism coupling technique. The films showed good optical homogeneity along the thickness direction by analyzing the guided mode spectra using the i-WKB method. The films exhibited relatively low surface scattered losses of 0.93 dB/cm and 1.29 dB/cm for TE_0 and TM_0 modes at 1550 nm, respectively, which is very favorite for use in infrared waveguides. Appropriate geometry of the rib waveguide structure was computed using the effective index method. A rib waveguide based on $Ba_{0.7}Sr_{0.3}TiO_3$ thin film grown on MgO substrate was successfully fabricated by photolithographic patterning and dry etching. A single mode (TE_{00}) propagation along the rib was observed, which agrees well with the numerical calculation. Thin-film Mach-Zehnder waveguide modulator from the $Ba_{0.7}Sr_{0.3}TiO_3$/MgO heterostructures has also been demonstrated. The measured half-wave voltage V_π is 60 V and the effective E-O coefficient r_c^{eff} of this device is calculated to be 27.0 ×10^{-12} m/V at a wavelength of 1550 nm. Our results show that BST thin film optical modulator is attractive promising candidate for the practical applications in optical communications.

8. Acknowledgment

Financial supports from the Vice-Chancellor's postdoctoral fellowship program, The University of New South Wales (SIR50/PS16940) and Australian Research Council Discovery Project (Grant No. DP110104629) are acknowledged.

9. References

Adachi, H. & Wasa, K. (1991). Sputtering preparation of ferroelectric PLZT thin films and their optical applications. *IEEE Trans.Ultra. Ferro. Freq. Contr*. 38: 645-655.

Agrawal, G. P. (May 2004). *Lightwave Technology: Components and Devices*. John Wiley & Sons, ISBN: 978-0-471-21573-8, New York.

Bass, M. (September 1, 1994). *Handbook of Optics, Vol. 2: Devices, Measurements, and Properties Second Edition, McGraw-Hill Professional,* ISBN-13: 978-0070479746, *New York.*

Beckers, L.; Schubert, J.; Zander, W.; Ziesmann, J.; Echau, A.; Leinenbach P. & Buchal, Ch. (1998). Structural and optical characterization of epitaxial waveguiding $BaTiO_3$ thin films on MgO. *J. Appl. Phys*. 83: 3305-3310.

Blomqvist, M.; Khartsev, S. & Grishin, A. (2005). Electrooptic ferroelectric $Na_{0.5}K_{0.5}NbO_3$ films. *IEEE Photonics Tech. Lett.* 17:1638-1640.

Chan, K. Y.; Tsang, W. S.; Mak C. L.; Wong, K. H. & Hui, P. M. (2004). Effect of composition of $PbTiO_3$ on optical properties of (1-x)$PbMg_{1/3}Nb_{2/3}O_{3-x}$-$PbTiO_3$ thin films. *Phys. Rev. B*. 69: 144111.

Chen, C. L.; Garret, T.; Lin, Y.; Jiang, J. C.; Meletis, E. I.; Miranda, F. A.; Zhang, Z. & Chu, W. K. (2002). Interface structures and epitaxial behavior of ferroelectric (Ba, Sr)TiO_3 thin films. *Integr. Ferro*. 42: 165-172.

Chen, D.; Hafich, M.; Huber, J. & Kyonka, J. (1980). PLZT modulators for optical communications. *Ferroelectrics*, 27: 73-76.

Chiang, Kin. S. (1985). Construction of refractive index profiles of planar dielectric waveguides from the distribution of effective indexes. *J. Lightwave. Tech.* LT-3: 385-391.

Davis, E. A. & Mott, N. F. (1970). Conduction in non-crystalline systems. 5. Conductivity, optical absorption and photoconductivity in amorphous semiconductors. *Phil. Mag*. 22: 903.

Dogheche, E.; Lansiaux, X. & Remiens, D. (2003). *m*-line spectroscopy for optical analysis of thick $LiNbO_3$ layers grown on sapphire substrates by radio-frequency multistep sputtering. *J. Appl. Phys*. 93: 1165-1168.

Dogheche, E.; Rémiens, D. & Thierry, B. (1996). Optimum parameters in the design of electrooptic waveguide modulators using ferroelectric thin films. *Proc. 10th IEEE Int'l. Sym. Appl. Ferro*. 1: 61-64.

Fork, D. K.; Armani-Leplingard, F. & Kingston, J. J. (1995). Optical losses in ferroelectric oxide thin films: is there light at the end of the tunnel? *Mater. Res. Soc. Symp. Proc*. 361: 155-166.

Gopalakrishnan, G. K.; Burns, W. K.; McElhanon, R. W.; Bulmer, C. H.; Greenblatt, A. S. (1994). Performance and modeling of broadband $LiNbO_3$ travelling wave optical intensity modulators. *J. Lightwave Technol.* 12:1807–1819.

Graettinger, T. M.; Rou, S. H.; Ameen, M. S.; Auciello, O. & Kingon, A. I. (1991). Electro-optic characterization of ion beam sputter-deposited KNbO3 thin films. *Appl. Phys. Lett*. 58: 1964-1966.

Guarino, A.; Poberaj, G.; Rezzonico, D.; Degl'innocenti, R. & Günter, P. (2007). Electro-optically tunable microing resonators in lithium niobate. *Nature Photonics*. 1: 407-410.

Haertling, G. H. (1987). PLZT electrooptic materials and applications-a review. *Ferroelectrics*, 75: 25-55.

Hoerman, B. H.; Nichols, B. M. & Wessels, B. W. (2003). The electro-optic properties of epitaxial $KTa_xNb_{1-x}O_3$ thin films. *Opt. Commun*. 219: 377-382.

Kang, T. D.; Xiao, B.; Avrutin, V.; Özgür, Ü.; Morkoç, H.; Park, J. W.; Lee, H. S.; Lee, H.; Wang, X. Y. & Smith, D. J. (2008). Large electro-optic effect in single-crystal Pb(Zr, Ti)O_3 (001) measured by spectroscopic ellipsometry. *J. Appl. Phys*. 104: 093103.

Kim, D. H. & Kwok, H. S. (1995). Pulsed laser deposition of $BaTiO_3$ thin films and their optical properties. *Appl. Phys. Lett*. 67: 1803-1805.

Kim, D. Y.; Moon, S. E.; Kim, E. K.; Lee, S. J.; Choi, J. J. & Kim, H. E. (2003). Electro-optic characteristics of (001)-oriented $Ba_{0.6}Sr_{0.4}TiO_3$ thin films. *Appl. Phys. Lett*. 82: 1455-1457.

Kogelnik, H. & Ramaswamy, V. (1974). Scaling rules for thin-film optical waveguides. *Appl. Opt*. 13: 1857-1862.

Krijnen, G. J. M.; Villeneuve, A.; Stegeman, G. I.; Aitchison, S.; Lambeck, P. & Hoekstra, J. W. M. (1995). Modelling of a versatile all-optical Mach-Zehnder switch. In: *Guided-Wave Optoelectronics: Device Characterization, Analysis, and Design*. Tamir, T.; Griffel, G. & Bertoni, H. F. pp. 187-196, Springer, ISBN-13: 978-0306451072, New York.

Lee, S. H.; Noh, T. W. & Lee, J. H. (1996). Control of epitaxial growth of pulsed laser deposited $LiNbO_3$ films and their electro-optic effects. *Appl. Phys. Lett*. 68: 472-474.

Li, J. W.; Duewer, F.; Gao, C.; Chang, H.; Xiang, X. D. & Lu, Y. L. (2000). Electro-optic measurements of the ferroelectric-paraelectric boundary in $Ba_{1-x}Sr_xTiO_3$ materials chips. *Appl. Phys. Lett*. 76: 769-771.

Lin, P. T.; Liu, Z. & Wessels, B. W. (2009). Ferroelectric thin film photonic crystal waveguide and its electro-optic properties. *J. Opt. A: Pure Appl. Opt*. 11: 075005.

Lu, Y. L.; Jin, G.-H.; Golomb, M. C.; Liu, S.-W.; Jiang, H.; Wang, F.-L.; Zhao, J.; Wang, S. –Q. & Drehman, A. J. (1998). Fabrication and optical characterization of $Pb(Mg_{1/3}Nb_{2/3})O_3$-$PbTiO_3$ planar thin film optical waveguides. *Appl. Phys. Lett*. 72: 2927-2929.

Lu, Y. L.; Zheng, J. J.; Golomb, M. C.; Wang, F. L.; Jiang, H. & Zhao, J. (1999). In-plane electro-optic anisotropy of (1-x)$Pb(Mg_{1/3}Nb_{2/3})O_3$-x$PbTiO_3$ thin films grown on (001)-cut $LaAlO_3$. *Appl. Phys. Lett*. 74: 3764-3766.

Manifacier, J. C.; Gasiot, J. & Fillard, J. P. (1976). A simple method for the determination of the optical constants n, k and the thickness of a weakly absorbing thin film. J. Phys. E: Sci. Instrum. 9: 1002-1004.

Marple, D. T. F. (1966). Optical absorption edge in CdTe: experimental. *Phys. Rev*. 150: 728-734.

Masuda, S.; Seki, A. & Masuda, Y. (2010). Influence of crystal phases on electro-optic properties of epitaxially grown lanthanum-modified lead zirconate titanate films. *Appl. Phys. Lett*. 96: 072901.

Masuda, S.; Seki, A.; Shiota, K. & Masuda, Y. (2011). Mach-Zehnder interferometer-type photonic switches based on epitaxially grown lanthanum-modified lead zirconate titanate films. *J. Lightwave Technol*. 29: 209-213.

Moon, S. E.; Kim, E. K.; Kwak, M. H.; Ryu, H. C.; Kim, Y. T.; Kang, K. Y.; Lee, S. J. &. Kim, W. J. (2003). Orientation dependent microwave dielectric properties of ferroelectric $Ba_{1-x}Sr_xTiO_3$ thin films. *Appl. Phys. Lett*. 83: 2166-2168.

Nakada, M.; Shimizu, T.; Miyazaki, H.; Tsuda, H.; Akedo, J. & Ohashi, K. (2009). Lanthanum-modified lead zirconate titanate electro-optic modulators fabricated using aerosol deposition for LSI interconnects. *Jpn. J. Appl. Phys*. 48: 09KA06.

Nashimoto, K.; Nakamura, S.; Morikawa, T.; Moriyama, H.; Watanabe, M. & Osakabe, E. (1999). Electrooptical properties of heterostructure (Pb, La)(Zr, Ti)O_3 waveguides on Nb–$SrTiO_3$. *Jpn. J. Appl. Phys*. 38: 5641-5645.

Petraru, A.; Schubert, J.; Schmid, M. & Buchal, Ch. (2002). Ferroelectric $BaTiO_3$ thin-film optical waveguide modulators. *Appl. Phys. Lett*. 81: 1375-1377.

Ramaswamy, V. (1974). Propagation in asymmetrical anisotropic film waveguides. *Appl. Opt*. 13: 1363-1371.

Suzuki, M.; Nagata, K. & Yokoyama, S. (2008). Imprint properties of optical Mach-Zehnder interferometers using (Ba, Sr)TiO_3 sputter-deposited at 450 °C. *Jpn. J. Appl. Phys*. 47: 2879-2901.

Tang, P. S.; Meier, A. L.; Towner, D. J. & Wessels, B. W. (2005). $BaTiO_3$ thin-film waveguide modulator with a low voltage–length product at near-infrared wavelengths of 0.98 and 1.55 μm. *Opt. Lett*. 30: 254-256.

Tauc, J. (1972). Optical properties of non-crystalline solids, In: *Optical Properties of Solids, Abeles, F. pp. 277, North-Holland,* ISBN-13: 978-0444100580*, Amsterdam*.

Tayebati, P.; Trivedi, D. & Tabat, M. (1996). Pulsed laser deposition of SBN:75 thin films with electro-optic coefficient of 844 pm/V. *Appl. Phys. Lett*. 69: 1023-1025.

Thielsch, R.; Kaemmer, K.; Holzapfel, B. & Schultz, L. (1997). Structure-related optical properties of laser-deposited $Ba_xSr_{1-x}TiO_3$ thin films grown on MgO (001) substrates. *Thin Solid Films*. 301: 203-210.

Tian, H. Y.; Choi, J.; No, K.; Luo, W. G. & Ding, A. L. (2002). Effect of compositionally graded configuration on the optical properties of $Ba_xSr_{1-x}TiO_3$ thin films derived from a solution deposition route. *Mater. Chem. Phys*. 78: 138-143.

Uchiyama, K.; Kasamatsu, A.; Otani, Y. & Shiosaki, T. (2007). Electro-optic properties of lanthanum-modified lead zirconate titanate thin films epitaxially grown by the advanced sol-gel method. *Jpn. J. Appl. Phys*. 46: L244-246.

Vilquin, B.; Bouregba, R.; Poullain, G.; Murray, H.; Dogheche, E. & Remiens, D. (2003). Crystallographic and optical properties of epitaxial $Pb(Zr_{0.6},Ti_{0.4})O_3$ thin films grown on $LaAlO_3$ substrates. *J. Appl. Phys*. 94: 5167-5171.

Walker, F. J.; McKee, R. A.; Yen, Huan-wun. & Zelmon, D. E. (1994). Optical clarity and waveguide performance of thin film perovskites on MgO. *Appl. Phys. Lett*. 65: 1495-1497.

Wan, X. M.; Luo, H. S.; Zhao, X. Y.; Wang, D. Y.; Chan, H. L. W. & Choy, C. L. (2004). Refractive indices and linear electro-optic properties of (1-x)$Pb(Mg_{1/3}Nb_{2/3})O_3$-x$PbTiO_3$ single crystals. *Appl. Phys. Lett*. 85: 5233-5235.

Wan, X. M.; Zhao, X. Y.; Chan, H. L. W.; Choy, C. L. & Luo, H. S. (2005). Crystal orientation dependence of the optical band gap of (1-x)$Pb(Mg_{1/3}Nb_{2/3})O_{3-x}$-$PbTiO_3$ single crystals. *Mater. Sci. Phys*. 92: 123-127.

Wang, D. Y.; Wang, Y.; Zhou, X. Y.; Chan, H. L. W. & Choy, C. L. (2005). Enhanced in-plane ferroelectricity in $Ba_{0.7}Sr_{0.3}TiO_3$ thin films grown on MgO (001) single-crystal substrate. *Appl. Phys. Lett*. 86: 212904.

Wang, D. Y.; Chan, H. L. W. & Choy, C. L. (2006a). Fabrication and characterization of epitaxial $Ba_{0.7}Sr_{0.3}TiO_3$ thin films for optical waveguide applications. *Appl. Opt*. 45: 1972-1978.

Wang, D. Y.; Lor, K. P.; Chung, K. K.; Chan, H. P.; Chiang, K. S.; Chan, H. L. W. & Choy, C. L. (2006b). Optical Rib Waveguide Based on Epitaxial $Ba_{0.7}Sr_{0.3}TiO_3$ Thin Film Grown on MgO, *Thin Solid Films*. 510: 329-333.

Wang, D. Y.; Wang, J.; Chan, H. L. W. & Choy, C. L. (2007a). Structural and electro-optic properties of $Ba_{0.7}Sr_{0.3}TiO_3$ thin films grown on various substrates using pulsed laser deposition. *J. Appl. Phys*. 101: 043515.

Wang, D. Y.; Lor, K. P.; Chung, K. K.; Chan, H. P.; Chiang, K. S.; Chan, H. L. W. & Choy, C. L. (2007b). Mach-Zehnder electro-optic modulator based on epitaxial $Ba_{0.7}Sr_{0.3}TiO_3$ thin films, *Ferroelectrics*, 357: 109-114.

Wang, D. Y.; Li, S.; Chan, H. L. W. & Choy, C. L. (2010). Optical and electro-optic anisotropy of epitaxial $Ba_{0.7}Sr_{0.3}TiO_3$ thin films. *Appl. Phys. Lett*. 96, 061905.

Wessles, B. W.; Nystrom, M. J.; Chen, J.; Studebaker, D. & Marks, T. J. (1996). Epitaxial niobate thin films and their nonlinear optical properties. *Mat. Res. Soc. Symp. Proc*. 401: 211-218.

Wessels, B. W. (2004). Thin Film Ferroelectrics for Guided Wave Devices. *J. Electroceramics*. 13: 135-138.

Wessels, B. W. (2007). Ferroelectric epitaxial thin films for integrated optics. *Annu. Rev. Mater. Res*. 37: 659-679.

Wooten, E. L.; Kissa, K. M.; Yi-Yan, A.; Murphy, E. J.; Lafaw, D. A.; Hallemeier, P. F.; Maack, D.; Attanasio, D. V.; Fritz, D. J.; McBrien, G. J. & Bossi, D. E. (2000). A review of lithium niobate modulators for fiber optic communication systems. *IEEE J. Sel. Top. Quant. Electron.* 6:69–82.

Xu, Y. (November 1, 1991). *Ferroelectric Materials and Their Applications*. North-Holland, ISBN-13: 978-0444883544, Amsterdam.

Yang, S. H.; Mo, D.; Tian, H. Y.; Luo, W.G.; Pu, X. H. & Ding, A. L. (2002). Spectroscopic ellipsometry of $Ba_xSr_{1-x}TiO_3$ thin films prepared by the sol–gel method. *Phys. Stat. Sol. (a)*. 191: 605-612.

Yariv, A. & Yeh, P. (1983). *Optical waves in crystals: propagation and control of laser radiation*. John Wiley & Sons, ISBN 13: 9780471091424, New York.

Zhu, M. M.; Du, Z. H. & Ma, J. (2010). Influence of crystal phase and transparent substrate on electro-optic properties of lead zirconate titanate films. *J. Appl. Phys*. 108: 113119.

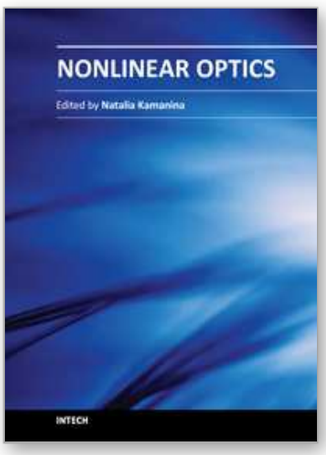

Nonlinear Optics

Edited by Dr. Natalia Kamanina

ISBN 978-953-51-0131-4
Hard cover, 224 pages
Publisher InTech
Published online 29, February, 2012
Published in print edition February, 2012

Rapid development of optoelectronic devices and laser techniques poses an important task of creating and studying, from one side, the structures capable of effectively converting, modulating, and recording optical data in a wide range of radiation energy densities and frequencies, from another side, the new schemes and approaches capable to activate and simulate the modern features. It is well known that nonlinear optical phenomena and nonlinear optical materials have the promising place to resolve these complicated technical tasks. The advanced idea, approach, and information described in this book will be fruitful for the readers to find a sustainable solution in a fundamental study and in the industry approach. The book can be useful for the students, post-graduate students, engineers, researchers and technical officers of optoelectronic universities and companies.

InTech Europe
University Campus STeP Ri
Slavka Krautzeka 83/A
51000 Rijeka, Croatia
Phone: +385 (51) 770 447
Fax: +385 (51) 686 166
www.intechopen.com

InTech China
Unit 405, Office Block, Hotel Equatorial Shanghai
No.65, Yan An Road (West), Shanghai, 200040, China
中国上海市延安西路65号上海国际贵都大饭店办公楼405单元
Phone: +86-21-62489820
Fax: +86-21-62489821

IntechOpen